MATLAB Functions for Mie Scattering and Absorption

Version 2

Christian Mätzler

Research Report No. 2002-11
August 2002

Institut für Angewandte Physik — Mikrowellenabteilung

Sidlerstrasse 5
3012 Bern
Schweiz

Tel. : +41 31 631 89 11
Fax. : +41 31 631 37 65
E-mail : matzler@iap.unibe.ch

MATLAB Functions for Mie Scattering and Absorption

Version 2

Christian Mätzler, Institute of Applied Physics, University of Bern, August 2002

List of Contents

Abstract

A set of MATLAB Functions for Mie calculations (Mätzler, 2002a) and for applications to microwave radiation in rain (Mätzler, 2002b) has been improved and expanded by including magnetic and metal-like media and coated spheres. The appendix includes a discussion of the basic behaviour or the Riccati-Bessel and related Functions needed in the computations of Mie Coefficients.
The applications of the Mie Functions are directed toward the study of radiative properties of precipitation. Functions have been developed to compute propagation parameters for freezing rain and melting graupel, assuming Marshall-Palmer drop-size distribution, including functions to compute the complex dielectric permittivities of ice and water. Other applications can be envisaged if the dielectric or refractive properties of the particles and their size distributions are known.

1 Introduction

This report is an extension of Mie-scattering and -absorption programs (Mätzler, 2002a) and applications to propagation, scattering and emission of microwave radiation in precipitation (Mätzler, 2002b) written in the numeric computation and visualisation software, MATLAB (Math Works, 1992). Mie Theory is based on the formulation of Bohren and Huffman (1983), in short BH. There and here the assumed time variation of the fields is $\exp(-i\omega t)$, leading to positive imaginary parts of the refractive index for absorbing media. For corresponding equations, equation numbers refer to those in BH or to page numbers of BH. In addition, for absorption by the internal electrical and magnetic fields, see Section 3.6 of the present report. For descriptions of computational problems in the Mie calculations, see the notes on p. 126-129, in Appendices A and B of BH and in the Appendix of this report which includes a description of the relevant functions (Riccati-Bessel functions and combinations thereof) and of their numerical behaviour.
Microwave interaction with precipitation mainly refers to Sauvageot (1992) and to Mätzler (2002b), including references therein.
Descriptions of the functions are given in Section 3, followed by some examples in Section 4.

2 Overview of changes with respect to Version 1

First of all, with respect to Mätzler (2002a), the parameter range was extended to larger size parameters in case of large imaginary refractive index (metal-like spheres) by replacing the function Mie_abcd for the Mie Coefficients a_n, d_n, c_n, d_n by two separate functions with improved algorithms, Mie_ab to compute a_n, b_n and Mie_cd for c_n, d_n.
Second, the new version allows for magnetic materials, by using the alternative functions Mie2_ab for a_n, b_n, and Mie2_cd for c_n, d_n. Functions starting with the name Mie2… refer to magnetic spheres with media properties given by mu1= μ_1/μ and eps1=$\varepsilon_1/\varepsilon$, where ε and μ are the permittivity and permeability of the ambient medium and ε_1 and μ_1 are the parameters of the sphere. For nonmagnetic spheres i.e. for $\mu_1=\mu$, there is a single medium-parameter (as in Version 1), the refractive index m relative to the ambient medium. This is the case for MATLAB functions starting with Mie… (i.e. without 2). The old function, Mie_abcd, of Version 1 is still included to enable numerical comparisons.
Third, the function Mie(m,x) returns the Mie Efficiencies (*Qext, Qsca, Qabs, Qb,* <*costeta*>), but no more the input parameters. The same is true for the respective functions, Mie2 and Miecoated. In this way the output of these three functions gets the same format.
Forth, the new version also includes functions for coated spheres with inner radius a (size parameter $x=ka$) and outer radius b (size parameter $y=kb$). The kernel has a refractive index m_1, and the coating has m_2, both relative to the ambient medium. Non-magnetic media are assumed as in BH. The name of such functions start with 'Miecoated'.
Finally, freezing rain and melting graupel, both with Marshall-Palmer drop-size distribution, are also included, see the functions Miecoated_rain*i*, where *i* is a number. These functions expand the microwave applications of rain (Mätzler, 2002b) to other forms of precipitation. Without difficulty, other size distributions can be introduced (e.g. Sauvageot, 1992, Section 2.2).

3 Functions and computational procedures

3.1 Mie Coefficients for homogeneous spheres

MATLAB Functions:
Mie_ab(m, x) produces a_n and b_n, for n=1 to n_{max} for non-magnetic spheres
Mie_cd(m, x) produces c_n and d_n, for n=1 to n_{max} for non-magnetic spheres
Mie2_ab(eps1, mu1, x) produces a_n and b_n, for n=1 to n_{max} for magnetic spheres
Mie2_cd(eps1, mu1, x) produces c_n and d_n, for n=1 to n_{max} for magnetic spheres
Mie_abcd(m, x) produces a_n, b_n, c_n and d_n, for n=1 to n_{max} for non-magnetic spheres (from Version 1)

The key parameters for Mie calculations are the Mie Coefficients a_n and b_n to compute the amplitudes of the scattered field, and c_n and d_n for the internal field, respectively. The coefficients are given in BH on p.100. First, the coefficients of the scattered electrical field are:

$$a_n = \frac{\mu m^2 j_n(mx)[xj_n(x)]' - \mu_1 j_n(x)[mxj_n(mx)]'}{\mu m^2 j_n(mx)[xh_n^{(1)}(x)]' - \mu_1 h_n^{(1)}(x)[mxj_n(mx)]'}$$
$$b_n = \frac{\mu_1 j_n(mx)[xj_n(x)]' - \mu j_n(x)[mxj_n(mx)]'}{\mu_1 j_n(mx)[xh_n^{(1)}(x)]' - \mu h_n^{(1)}(x)[mxj_n(mx)]'} \qquad (4.53)$$

where prime means derivative with respect to the argument; similar expressions exist for the coefficients c_n and d_n of the internal field (see below). The Index n runs from 1 to ∞, but the infinite series occurring in Mie formulas can be truncated at a maximum, n_{max}; for this number Bohren and Huffman (1983) proposed

$$n_{\max} = x + 4x^{1/3} + 2 \qquad \text{(p.477)}$$

and this value is used here as well. The size parameter is given by $x=ka$, a is the radius of the sphere and $k = 2\pi/\lambda$ is the wave number, λ the wavelength in the ambient medium, $m=(\varepsilon_1\mu_1)^{1/2}/(\varepsilon\mu)^{1/2}$ is the refractive index with respect to the ambient medium, ε_1 and μ_1 are the permittivity and permeability of the sphere and ε and μ are the permittivity and permeability of the ambient medium. The functions $j_n(z)$ and $h_n^{(1)}(z) = j_n(z) + iy_n(z)$ are spherical Bessel functions of order n and of the given arguments, $z = x$ or mx, respectively. The derivatives follow from the spherical Bessel functions themselves, namely

$$[zj_n(z)]' = zj_{n-1}(z) - nj_n(z);\ [zh_n^{(1)}(z)]' = zh_{n-1}^{(1)}(z) - nh_n^{(1)}(z) \qquad \text{(p.127)}$$

Relationships exist between Bessel and spherical Bessel functions:

$$j_n(z) = \sqrt{\frac{\pi}{2z}} J_{n+0.5}(z) \qquad (4.9)$$

$$y_n(z) = \sqrt{\frac{\pi}{2z}} Y_{n+0.5}(z) \qquad (4.10)$$

Here, J_ν and Y_ν are Bessel functions of the first and second kind; for n=0 and 1 the spherical Bessel functions are simply given (BH, p. 87) by

$$j_0(z) = \sin z / z; \quad j_1(z) = \sin z / z^2 - \cos z / z$$
$$y_0(z) = -\cos z / z; \quad y_1(z) = -\cos z / z^2 - \sin z / z$$

and the recurrence formula can be used to obtain higher orders

$$f_{n-1}(z)+f_{n+1}(z)=\frac{2n+1}{z}f_n(z) \tag{4.11}$$

where f_n is any of the functions j_n and y_n. Power-series expansions for small arguments of j_n and y_n are given on p. 130 of BH. The spherical Hankel Functions are linear combinations of j_n and y_n. Here, the first type is required

$$h_n^{(1)}(z)=j_n(z)+iy_n(z) \tag{4.13}$$

The related Riccati-Bessel Functions will also be used:

$$\psi_n(z)=zj_n(z);\ \chi_n(z)=-zy_n(z);\ \xi_n(z)=zh_n^{(1)}(z) \qquad \text{(p.101, 183)}$$

By transforming (4.53) we get expressions corresponding to (4.88) in BH, but now allowing μ_1 to be different from μ. Under certain conditions these expressions are more suitable for numerical computations; at the same time, the most delicate functions, $\psi_n(mx)=mx\cdot j_n(mx)$, and their derivatives are eliminated in the equations for the scattered field (Mie_ab and Mie2_ab). As shown in the Appendix, the function $\psi_n(mx)$ and its derivative diverge for lossy media, and the effect is especially strong for, metals (the reason for the limited range of application in Version 1). On the other hand, the logarithmic derivative D_n of ψ_n

$$D_n=\frac{\psi_n'(mx)}{\psi_n(mx)}=\frac{[mx\cdot j_n(mx)]'}{mx\cdot j_n(mx)} \tag{1}$$

remains finite except for $x\to 0$. The function $D_n(z)$ with the complex argument $z=mx$ is computed as described in BH in Section 4.8, by downward recurrence

$$D_{n-1}(z)=\frac{n}{z}-\frac{1}{D_n(z)+n/z} \tag{2}$$

starting at n=nstart=round(max(n_{max},abs(z))+16), by using D_{nstart}=0, and ending at n=2. The values of D_1 to D_{nmax} are used by the MATLAB Function Mie(m, x) for $\mu_1=\mu$ and Mie2(eps1, mu1, x) for $\mu_1\neq\mu$, i.e. magnetic spheres.
Dividing nominator and denominator of the expression for a_n in (4.53) by $\psi_n(mx)=mx\cdot j_n(mx)$ we get

$$\begin{aligned}
a_n&=\frac{\mu m[xj_n(x)]'-\mu_1 xj_n(x)D_n(mx)}{\mu m[xh_n^{(1)}(x)]'-\mu_1 xh_n^{(1)}(x)D_n(mx)}\\
&=\frac{\psi_n'(x)-\psi_n(x)D_n(mx)\mu_1/(\mu m)}{\xi_n'(x)-\xi_n(x)D_n(mx)\mu_1/(\mu m)}\\
&=\frac{[D_n(mx)\mu_1/(\mu m)+n/x]\psi_n(x)-\psi_{n-1}(x)}{[D_n(mx)\mu_1/(\mu m)+n/x]\xi_n(x)-\xi_{n-1}(x)}\\
&=\frac{[D_n(mx)z_1+n/x]\psi_n(x)-\psi_{n-1}(x)}{[D_n(mx)z_1+n/x]\xi_n(x)-\xi_{n-1}(x)}
\end{aligned} \tag{3}$$

Correspondingly, using the same transformation, we get for b_n

$$b_n=\frac{[D_n(mx)/z_1+n/x]\psi_n(x)-\psi_{n-1}(x)}{[D_n(mx)/z_1+n/x]\xi_n(x)-\xi_{n-1}(x)} \tag{4}$$

The impedance and refractive-index ratios z_1 and m, respectively, between inside and outside of the sphere are given by

$$z_1 = \frac{\mu_1}{\mu m} = \frac{\sqrt{\mu_1/\varepsilon_1}}{\sqrt{\mu/\varepsilon}}; \quad m = \frac{\sqrt{\mu_1\varepsilon_1}}{\sqrt{\mu\varepsilon}} \tag{5}$$

The coefficients of the internal field, including magnetic effects, are given by

$$\begin{aligned} c_n &= \frac{\mu_1 j_n(x)[xh_n^{(1)}(x)]' - \mu_1 h_n^{(1)}(x)[xj_n(x)]'}{\mu_1 j_n(mx)[xh_n^{(1)}(x)]' - \mu h_n^{(1)}(x)[mxj_n(mx)]'} \\ d_n &= \frac{\mu_1 m j_n(x)[xh_n^{(1)}(x)]' - \mu_1 m h_n^{(1)}(x)[xj_n(x)]'}{\mu m^2 j_n(mx)[xh_n^{(1)}(x)]' - \mu_1 h_n^{(1)}(x)[mxj_n(mx)]'} \end{aligned} \tag{4.52}$$

Note that the function $j_n(mx)$ and its derivative cannot be eliminated in (4.52). However, as they appear in the denominator only, their divergence just leads to diminishing values of c_n and d_n.
The computation of the functions with the real argument x is done as in Version 1 by directly calling the MATLAB built-in Bessel Functions.

3.2 Mie Coefficients for coated spheres

MATLAB Functions: Miecoated_ab*opt*(m1, m2, x, y) produce a_n and b_n, for n=1 to n_{max} for Option *opt*=1, 2, 3.

Mie Coefficients a_n and b_n of coated spheres can be used in the same way as the ones for homogeneous spheres (BH, Section 8.1) to compute cross sections and scattering diagrams. The model of BH assumes non-magnetic materials. The coated sphere has an inner radius a with size parameter $x=ka$ (k is the wave number in the ambient medium) and m_1 is the inner-medium refractive index relative to the ambient medium, a coating of outer radius b with relative refractive index m_2, and size parameter $y=kb$.
One form (Option 1) used to compute the Mie Coefficients of coated spheres is the following (as presented in Appendix B of BH, p. 483):

$$a_n = \frac{(\widetilde{D}_n/m_2 + n/y)\psi_n(y) - \psi_{n-1}(y)}{(\widetilde{D}_n/m_2 + n/y)\xi_n(y) - \xi_{n-1}(y)}; \qquad b_n = \frac{(m_2\widetilde{G}_n + n/y)\psi_n(y) - \psi_{n-1}(y)}{(m_2\widetilde{G}_n + n/y)\xi_n(y) - \xi_{n-1}(y)}$$

$$\widetilde{D}_n = \frac{D_n(m_2y) - A_n\chi_n'(m_2y)/\psi_n(m_2y)}{1 - A_n\chi_n(m_2y)/\psi_n(m_2y)}; \quad \widetilde{G}_n = \frac{D_n(m_2y) - B_n\chi_n'(m_2y)/\psi_n(m_2y)}{1 - B_n\chi_n(m_2y)/\psi_n(m_2y)}$$

$$A_n = \psi_n(m_2x)\frac{mD_n(m_1x) - D_n(m_2x)}{mD_n(m_1x)\chi_n(m_2x) - \chi_n'(m_2x)};$$

$$B_n = \psi_n(m_2x)\frac{D_n(m_1x)/m - D_n(m_2x)}{D_n(m_1x)\chi_n(m_2x)/m - \chi_n'(m_2x)}; \qquad m = \frac{m_2}{m_1}$$

The computation of these coefficients can cause problems for certain combinations of the parameters (m1, m2, x, y) because of the diverging nature of some of the functions used (see e.g. Figures in the Appendix of this report and the discussion in Appendix B of BH). Therefore three different options are available for tests and comparisons. Under good conditions, the results of all options are the same. Problems are indicated if the results differ noticeably or if NaN values are returned. Option 1 uses the computation as formulated above, and the recurrence relation (4.89, p. 127) for the functions D_n. Careful treatment of diverging functions (e.g.

avoiding direct products of them) is applied. Option 2 uses the fromulation on p. 183 of BH. The same formulas are also used in Option 3, but for the derivatives χ_n' the equation at the bottom of p. 483, resulting from the Wronskian (4.60), is applied instead of the ordinary relationship (BH, p. 127). The selection of the Option is done by the Option Parameter, *opt*, in MATLAB Function Miecoated (see below). Standard Option used in the applications is *opt*=1.

3.3 Computation and plot of Mie Efficiencies

MATLAB functions:
Mie(m, x) produces *Qext, Qsca, Qabs, Qb,* <*costeta*>, for non-magnetic spheres
Mie2(eps1, mu1, x) produces *Qext, Qsca, Qabs, Qb,* <*costeta*>, for magnetic spheres
Miecoated(m1,m2,x,y,opt) produces *Qext, Qsca, Qabs, Qb,* <*costeta*>, for non-magnetic, coated spheres for size parameters x and y, of kernel and coating, repectively, Option (*opt*=1,2,3).
Mie_xscan(m, nsteps, dx) and Mie2_xscan(eps1, mu1, nsteps, dx) are used to plot the efficiencies versus size parameter x in a number (nsteps) of steps of increment dx from x=0 to x=nsteps·dx.
Miecoated_*i*scan(m1,m2,y,nsteps), where *i*=w, wr, pr are used to plot the efficiencies (for given y) versus volumetric fraction w of the coating, fractional thickness wr and pr of core and coating, respectively, and Option for Miecoated is *opt*=1.

The efficiencies Q_i for the interaction of radiation with a sphere of radius a are cross sections σ_i (called C_i in BH) normalised to the geometrical particle cross section, $\sigma_g=\pi a^2$, ($\sigma_g=\pi b^2$, in case of coated spheres), where i stands for extinction ($i=ext$), absorption ($i=abs$), scattering ($i=sca$), backscattering ($i=b$), and radiation pressure ($i=pr$), thus

$$Q_i = \frac{\sigma_i}{\sigma_g} \tag{6}$$

Energy conservation requires that

$$Q_{ext} = Q_{sca} + Q_{abs}\,, \quad \text{or} \quad \sigma_{ext} = \sigma_{sca} + \sigma_{abs} \tag{3.25}$$

The scattering efficiency Q_{sca} follows from the integration of the scattered power over all directions, and the extinction efficiency Q_{ext} follows from the Extinction Theorem (Ishimaru, 1978, p. 14, van de Hulst, 1957, p. 31), also called Forward-Scattering Theorem, leading to:

$$Q_{sca} = \frac{2}{x^2}\sum_{n=1}^{\infty}(2n+1)(|a_n|^2 + |b_n|^2) \tag{4.61}$$

$$Q_{ext} = \frac{2}{x^2}\sum_{n=1}^{\infty}(2n+1)\,\mathrm{Re}(a_n + b_n) \tag{4.62}$$

and Q_{abs} follows from (3.25). All infinite series can be truncated after n_{max} terms. Furthermore, the asymmetry parameter $g=\langle\cos\theta\rangle$ indicates the average cosine of the scattering angle θ with respect to power; it is used e.g. in Two-Stream Models (Meador and Weaver, 1980), and it is related to the efficiency Q_{pr} of radiation pressure:

$$Q_{pr} = Q_{ext} - Q_{sca}\langle\cos\theta\rangle \tag{p.120}$$

$$Q_{sca}\langle\cos\theta\rangle = \frac{4}{x^2}\left\{\sum_{n=1}^{\infty}\frac{n(n+2)}{n+1}\mathrm{Re}(a_n a_{n+1}^* + b_n b_{n+1}^*) + \sum_{n=1}^{\infty}\frac{2n+1}{n(n+1)}\mathrm{Re}(a_n b_n^*)\right\}$$

Finally, the backscattering efficiency Q_b, applicable to monostatic radar, is given by

$$Q_b = \frac{1}{x^2}\left|\sum_{n=1}^{\infty}(2n+1)(-1)^n(a_n - b_n)\right|^2 \qquad \text{(p.122)}$$

3.4 The scattered far field

MATLAB functions:

Mie_S12(m, x, u), Mie2_S12(eps1, mu1, x, u) to compute the functions S_1 and S_2 where u=cos(θ) for scattering angle θ

Mie_pt(u, nmax) to compute the angular functions $\pi_n(u)$ and $\tau_n(u)$, for n=1 to nmax. The same function is applicable to magnetic, non-magnetic and coated spheres.

Mie_tetascan(m, x, nsteps), Mie2_tetascan(eps1, mu1, x, nsteps) and Miecoated_tetascan(m1, m2, x, y, nsteps) are used to plot the scattered power versus scattering angle teta in a number (nsteps) of steps from 0 to 180° for non-magnetic and magnetic spheres, and for coated spheres, respectively. Mie scattering intensities $|S_1|^2$ and $|S_2|^2$ are plotted as a function of u=cosθ, the result being shown as a polar diagram of θ with $|S_1|^2$ in the upper half circle (0<θ<π) and $|S_2|^2$ in the lower half circle (π<θ<2π).

If the detailed shape of the angular scattering pattern is required, e.g. to get the phase matrix or phase function for radiative-transfer calculations (Chandrasekhar, 1960), the scattering functions S_1 and S_2 are required. These functions describe the scattered field $\mathbf{E_s}$. The scattered far field in spherical coordinates ($E_{s\theta}$, $E_{s\phi}$) for a unit-amplitude incident field (where the time variation exp(-iωt) has been omitted) is given by

$$\begin{aligned} E_{s\theta} &= \frac{e^{ikr}}{-ikr}\cos\phi \cdot S_2(\cos\theta) \\ E_{s\phi} &= \frac{e^{ikr}}{ikr}\sin\phi \cdot S_1(\cos\theta) \end{aligned} \qquad \text{(p.111)}$$

with the scattering amplitudes S_1 and S_2

$$\begin{aligned} S_1(\cos\theta) &= \sum_{n=1}^{\infty}\frac{2n+1}{n(n+1)}(a_n\pi_n + b_n\tau_n); \\ S_2(\cos\theta) &= \sum_{n=1}^{\infty}\frac{2n+1}{n(n+1)}(a_n\tau_n + b_n\pi_n) \end{aligned} \qquad (4.74)$$

$E_{s\theta}$ is the scattered far-field component in the scattering plane, defined by the incident and scattered directions, and $E_{s\phi}$ is the orthogonal component. The angle φ is the angle between the incident electric field and the scattering plane. The functions $\pi_n(\cos\theta)$ and $\tau_n(\cos\theta)$ describe the angular scattering patterns of the spherical harmonics used to describe S_1 and S_2 and follow from the recurrence relations

$$\pi_n = \frac{2n-1}{n-1}\cos\theta\cdot\pi_{n-1} - \frac{n}{n-1}\pi_{n-2};\ \ \tau_n = n\cos\theta\cdot\pi_n - (n+1)\pi_{n-1} \qquad (4.47)$$

starting with (Deirmendjian, 1969, p. 15)

$$\pi_0 = 0;\ \pi_1 = 1;\ \pi_2 = 3\cos\theta;\ \tau_0 = 0;\ \tau_1 = \cos\theta;\ \tau_2 = 3\cos(2\theta) \qquad (7)$$

3.5 The internal field

MATLAB function: presently, no direct function, but see Mie_Esquare and Mie2_Esquare below

The internal field $\mathbf{E}_1$ for an incident field with unit amplitude is given by

$$\mathbf{E}_1 = \sum_{n=1}^{\infty} \frac{2n+1)}{n(n+1)} \left(c_n \mathbf{M}_{o1n}^{(1)} - d_n \mathbf{N}_{e1n}^{(1)} \right) \tag{4.40}$$

where the vector-wave harmonic fields are given in spherical (r,θ,ϕ) coordinates by

$$\mathbf{M}_{o1n}^{(1)} = \begin{pmatrix} 0 \\ \cos\phi \cdot \pi_n(\cos\theta)\, j_n(rmx) \\ -\sin\phi \cdot \tau_n(\cos\theta)\, j_n(rmx) \end{pmatrix}$$

$$\mathbf{N}_{e1n}^{(1)} = \begin{pmatrix} n(n+1)\cos\phi \cdot \sin\theta \cdot \pi_n(\cos\theta) \dfrac{j_n(rmx)}{rmx} \\ \cos\phi \cdot \tau_n(\cos\theta) \dfrac{[rmx j_n(rmx)]'}{rmx} \\ -\sin\phi \cdot \pi_n(\cos\theta) \dfrac{[rmx j_n(rmx)]'}{rmx} \end{pmatrix} \tag{4.50}$$

and the coordinate system is defined as for the scattered field. The vector-wave functions **N** and **M** are orthogonal with respect to integration over directions. Furthermore for different values of n, the **N** functions are orthogonal, too, and the same is true for the **M** functions.

3.6 Computation of Q_{abs}, based on the internal fields

MATLAB functions:

Mie_Esquare(m, x, nj), Mie2_Esquare(eps1, mu1, x, nj) to compute nj values from 0 to x of the absolute-squared electrical field inside the sphere

Mie_abs(m, x), Mie2_abs(eps1, mu1, x) to compute the absorption coefficient, based on Ohmic losses (and including magnetic losses in case of Mie2_abs)

3.6.1 Dielectric losses only

The absorption cross section of a particle with dielectric (i.e. Ohmic) losses is given by (Ishimaru, 1978, p. 17)

$$\sigma_{abs} = k\varepsilon'' \int_V |\mathbf{E}_1|^2 dV \tag{8}$$

where ε" is the imaginary part of the relative dielectric constant of the particle (here with respect to the ambient medium). Thanks to the orthogonality of the spherical vector-wave functions this integral becomes in spherical coordinates

$$\sigma_{abs} = k\varepsilon'' \pi \sum_{n=1}^{\infty} \int_{-1}^{+1} d(\cos\theta) \int_0^a r^2 dr \left(|c_n|^2 (m_\theta + m_\phi) + |d_n|^2 (n_r + n_\theta + n_\phi) \right) \tag{9}$$

and the integration over azimuth ϕ has already been performed, leading to the factor π. The functions in the integrand are absolute-square values of the series terms of the components of the vector-waves (4.50)

$$
\begin{aligned}
m_\theta &= g_n \pi_n^2(\cos\theta)\cdot\left|j_n(z)\right|^2 \\
m_\phi &= g_n \tau_n^2(\cos\theta)\cdot\left|j_n(z)\right|^2 \\
n_r &= g_n \sin^2\theta\cdot\pi_n^2(\cos\theta)\left|\frac{j_n(z)}{z}\right|^2 \\
n_\theta &= g_n \tau_n^2(\cos\theta)\left|\frac{(zj_n(z))'}{z}\right|^2 \\
n_\phi &= g_n \pi_n^2(\cos\theta)\left|\frac{(zj_n(z))'}{z}\right|^2
\end{aligned}
\tag{10}
$$

Here $z=mrk$, and g_n stands for

$$g_n = \left(\frac{2n+1}{n(n+1)}\right)^2 \tag{11}$$

For the integrals over cosθ, analytic solutions can be obtained. First, from BH we find

$$\int_{-1}^{1}\left(\pi_n^2(\cos\theta)+\tau_n^2(\cos\theta)\right)d(\cos\theta)=\frac{2n^2(n+1)^2}{2n+1} \tag{p.103}$$

and second, from (4.46) in BH and Equation 8.14.13 of Abramowitz and Stegun (1965), we get

$$\int_{-1}^{1}\left(\sin^2\theta\cdot\pi_n^2(\cos\theta)\right)d(\cos\theta)=\int_{-1}^{1}\left(P_n^1(\cos\theta)\right)^2 d(\cos\theta)=\frac{2(n+1)}{2n+1} \tag{12}$$

leading to the two parts (13) and (14) of the angular integral in (9)

$$m_n=\int_{-1}^{1}\left(m_\theta+m_\phi\right)d(\cos\theta)=2(2n+1)\left|j_n(z)\right|^2 \tag{13}$$

$$n_n=\int_{-1}^{1}(n_r+n_\theta+n_\phi)d(\cos\theta)=2n(2n+1)\left\{(n+1)\left|\frac{j_n(z)}{z}\right|^2+\left|\frac{(zj_n(z))'}{z}\right|^2\right\} \tag{14}$$

Now, the absorption cross section follows from integration over the radial distance r inside the sphere up to the sphere radius a:

$$\sigma_{abs}=k\varepsilon''\pi\sum_{n=1}^{\infty}\int_0^a\left(m_n\left|c_n\right|^2+n_n\left|d_n\right|^2\right)\cdot r^2 dr \tag{15}$$

The integrand contains the radial dependence of the absolute-square electric field $\left\langle\left|\mathbf{E}\right|^2\right\rangle$ averaged over spherical shells (all θ and ϕ, constant r):

$$\left\langle\left|\mathbf{E}\right|^2\right\rangle=\frac{1}{4}\sum_{n=1}^{\infty}\left(m_n\left|c_n\right|^2+n_n\left|d_n\right|^2\right) \tag{16}$$

and in terms of this quantity, the absorption efficiency becomes

$$Q_{abs} = \frac{4\varepsilon''}{x^2}\int_0^x \left\langle |\mathbf{E}|^2 \right\rangle x'^2\, dx' \tag{17}$$

where $x'=rk=z/m$. Note that (16) is dimensionless because of the unit-amplitude incident field; In case of Rayleigh scattering ($x<<1$) the internal field is constant, and the corresponding squared-field ratio (16) is given by

$$\frac{9}{\left|m^2+2\right|^2} \tag{18}$$

This quantity can be used to test the accuracy of the function, Mie_Esquare, for small size parameters. In addition, Equation (17) or (19) can be used to test the accuracy of the computation of Q_{abs} from the difference, $Q_{ext} - Q_{sca}$ (4.61-62). Finally, it should be noted again that all infinite series can be terminated after n_{max} terms.

3.6.2 Dielectric and magnetic losses

For spheres including magnetic losses, the absorption efficiency also includes a magnetic current, the equivalent term due to the imaginary part μ"=imag(μ1/μ) of the magnetic permeability. By duality (Kong, 1986), the electrical field **E** has to be replaced by the magnetic field **H**, thus

$$Q_{abs} = \frac{4\varepsilon''}{x^2}\int_0^x \left\langle |\mathbf{E}|^2 \right\rangle x'^2\, dx' + \frac{4\mu''}{x^2}\int_0^x \left\langle |\mathbf{H}|^2 \right\rangle x'^2\, dx' \tag{19}$$

and $\left\langle |\mathbf{H}|^2 \right\rangle$ is obtained by interchanging μ_1/μ=mu1 and $\varepsilon_1/\varepsilon$=eps1, i.e. calling Mie2_Esquare(mu1, eps1, x, nj).

3.7 Dielectric functions for water and ice

MATLAB Functions

Computation of complex refractive index: m*i*=sqrt(eps*i*), where *i*=ice or water:

epswater(fGHz, TK): complex permittivity of water according to Liebe et al. (1991), at frequency fGHz in GHz and temperature TK in Kelvin.

epsice(fGHz, TK): complex permittivity of ice according to Mätzler (1998), at frequency fGHz in GHz and temperature TK in Kelvin.

The above functions are applicable over a frequency range of at least 1 to 1000 GHz and for appropriate temperatures of the atmosphere (100 to 273K for water ice, 250 to 320 K for liquid water). Impurities are not taken into account here.

4 Examples and Tests

4.1 The situation of x=1, m=1000+1000i

Metals are characterised by large imaginary permittivity; the chosen value is an example of a metal-like sphere for which Mie_abcd of Version 1 returned NaN values. Now, the execution of the command line

>> m =1000 + 1000i; x = 1; mie_ab(m,x)

returns the vectors [a_n; b_n] for n=1 to n_{max}=7: ans = Columns 1 through 4

```
  0.2926 - 0.4544i   0.0009 - 0.0304i   0.0000 - 0.0008i   0.0000 - 0.0000i
  0.0455 + 0.2077i   0.0003 + 0.0172i   0.0000 + 0.0005i   0.0000 + 0.0000i
```

Columns 5 through 7

0.0000 - 0.0000i 0.0000 - 0.0000i 0.0000 - 0.0000i
0.0000 + 0.0000i 0.0000 + 0.0000i 0.0000 + 0.0000i

whereas the function mie_cd(m,x) returns zeros.

4.2 Magnetic sphere with x=2, eps1=2+i, mu1=0.8+0.1i

The command line
>> eps1=2+1i; mu1=0.8+0.1i; x=2; mie2_ab(eps1,mu1,2)
leads to the Mie Coefficients: ans = Columns 1 through 4

0.3745 - 0.1871i 0.1761 - 0.1301i 0.0178 - 0.0237i 0.0010 - 0.0016i
0.3751 + 0.0646i 0.0748 + 0.0294i 0.0068 + 0.0044i 0.0004 + 0.0003i

Columns 5 through 8

0.0000 - 0.0001i 0.0000 - 0.0000i 0.0000 - 0.0000i 0.0000 - 0.0000i
0.0000 + 0.0000i 0.0000 + 0.0000i 0.0000 + 0.0000i 0.0000 + 0.0000i

Column 9

0.0000 - 0.0000i
0.0000 + 0.0000i

whereas the command line
>>mie2(eps1,mu1,2)
returns the Mie Efficiencies Qext, Qsca, Qabs, Qb, <costeta> and Qb/Qsca
ans = 1.8443 0.6195 1.2248 0.0525 0.6445 0.0847

and the command line
>>mie2_abs(eps1,mu1,2)
gives the absorption efficiency by the alternative way

Qabse = 0.9630
Qabsm = 0.2618
ans = 1.2248

Here Qabse is the absorption efficiency due to the electrical field (Ohmic losses), Qabsm due to the magnetic field, and ans is the sum, i.e. the total absorption efficiency, in agreement with the third number of the result of Mie2(eps1, mu1, x), s. above.

Mie Efficiencies are plotted versus x ($0 \le x \le 5$) by Mie2_xscan(eps1, mu1, 501, 0.01) in Fig. 1. To plot the angular dependence of the scattered power in the two polarisations, the function Mie2_tetascan(eps1,mu1,x,201), for x=0.2, is used to provide Figure 2.
Furthermore the absolute-square internal **E** and **H** fields are plotted versus the radial distance at x=5 by calling Mie2_Esquare(eps1,mu1,x,201) for **E** in Figure 3 (left) and Mie2_Esquare(mu1, eps1,x,201) for **H** in Figure 3 (right).

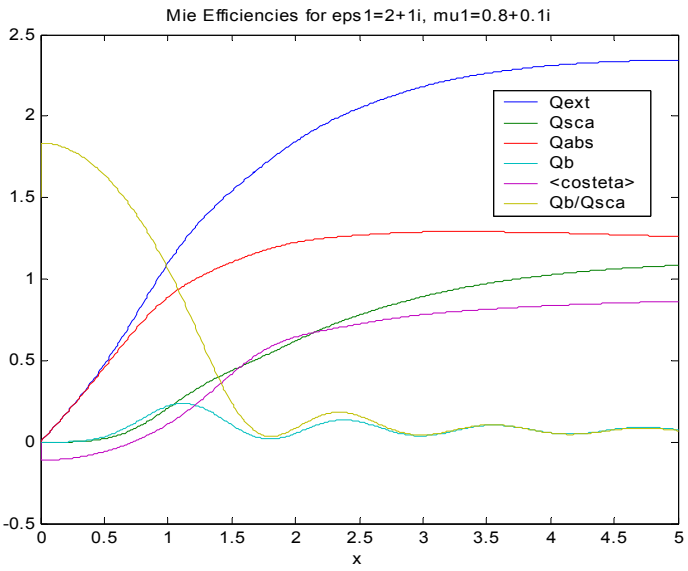

Figure 1: Mie Efficiencies for *eps1*=1+i, *mu1*=0.8+0.1i, versus *x*, output of the function, Mie2_xscan.

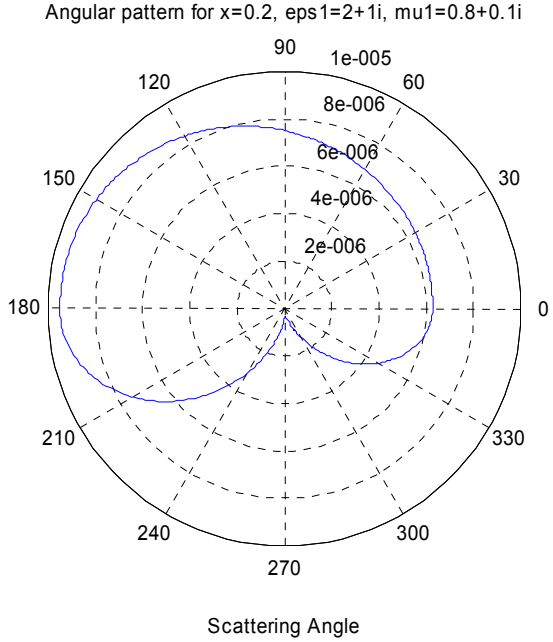

Figure 2 (left): Angular Mie-scattering diagram of $|S_1|^2$ (upper Half circle) and of $|S_2|^2$ (lower half circle) at *x*=0.2 and for the situation of Figure 1.

Figure 3 (below): Radial variation of the ratio of the internal/external absolute-square electric field (left) and magnetic field (right) with *x*=5 for the situation of Figure 1. Due to the skin effect, the field is concentrated near the edge of the sphere.

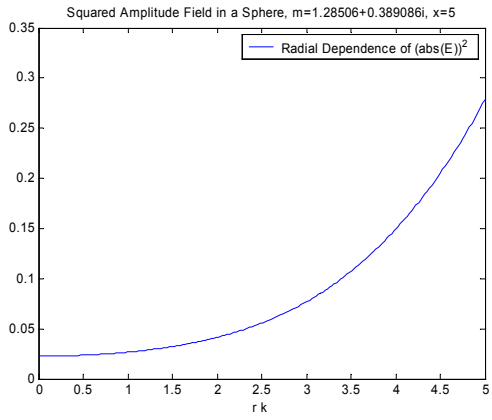

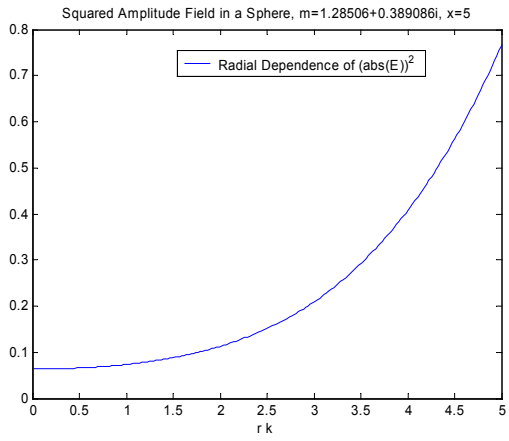

In contrast to non-magnetic spheres, the behaviour at low *x* values is different in Figure 1 where the ratio Q_b/Q_{sca} does not approach the Rayleigh result of 1.5 for non-magnetic spheres (Mätzler, 2002a). Here, the value is slightly larger. On the

other hand if *eps1=mu1* we get Q_b=0 for all values of *x*. An equivalent result is found for the reflection on a plane surface at vertical incidence where the reflection disappears for *eps1=mu1* because there is no impedance change.

4.3 Water-coated ice sphere

The following command produces a plot of Mie Efficiencies versus relative thickness of the coating for a water-coated ice sphere at 31 GHz, *y*=1, TK=273K (s. Figure 4):
>>miecoated_wrscan(sqrt(epsice(31,273)),sqrt(epswater(31,273)),1,4000)
Note the significant effect of very thin coatings of liquid water on absorption, here.

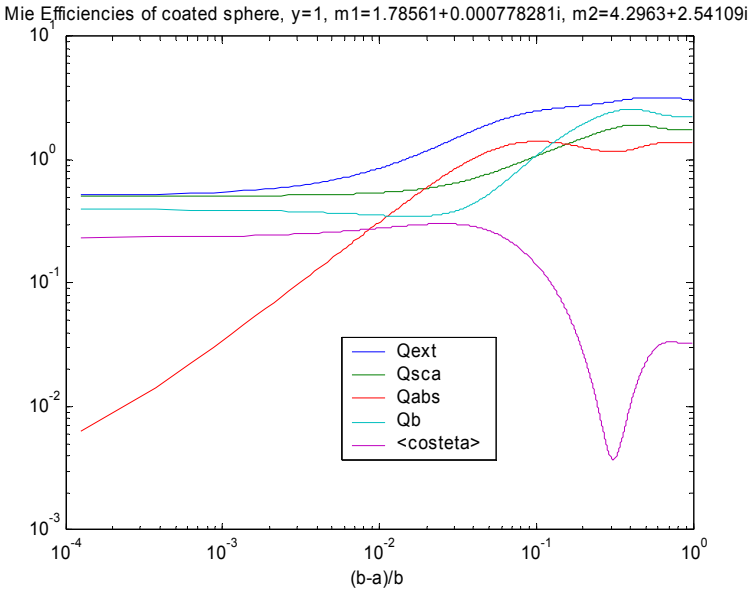

Figure 4: Mie Efficiencies versus relative thickness of coating for water-coated ice sphere of *y*=1 at 31 GHz, *T*=273K, i.e. *b*=1.54mm. Note the double-logarithmic scaling. Whereas the effect of liquid water on scattering disappears for very thin coatings, Q_{abs} is still affected.

4.4 Ice-coated water sphere

The following command produces a plot of Mie Efficiencies versus relative thickness of the coating for a water-coated ice sphere at 31 GHz, *y*=1, TK=273K (Figure 5):
>> miecoated_wrscan(sqrt(epswater(31,273)),sqrt(epsice(31,273)),1,4000)
In contrast to coatings of liquid water (Section 4.3), Figure 5 does not show a special sensitivity to thin coatings of ice.

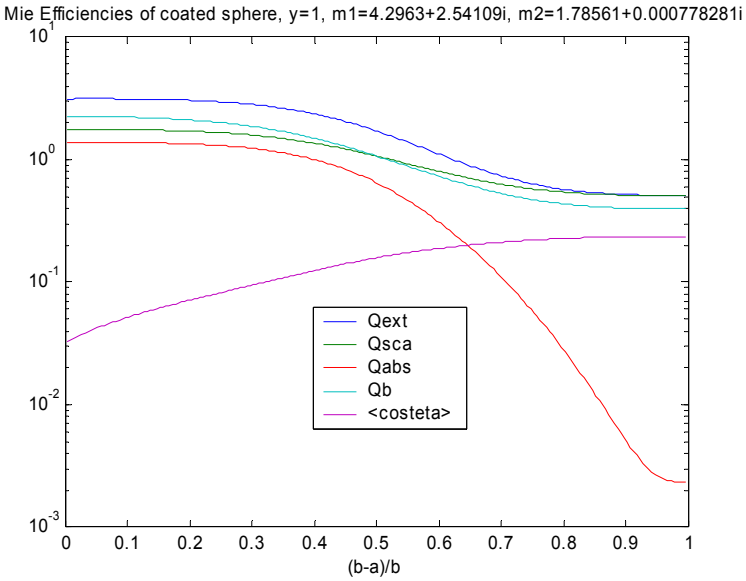

Figure 5: Mie Efficiencies versus relative thickness of water coating for an ice sphere of y=1 at 31 GHz, 273K, i.e. b=1.54mm. Note the logarithmic scale in the vertical axis and the linear scale in the horizontal axis.

4.5 Water bubble

Water bubbles appear as near black bodies (Q_{abs}>>Q_{sca}). An example is shown by
>> miecoated_wrscan(1, sqrt(epswater(31,273)),5,4000), see Figure 6.

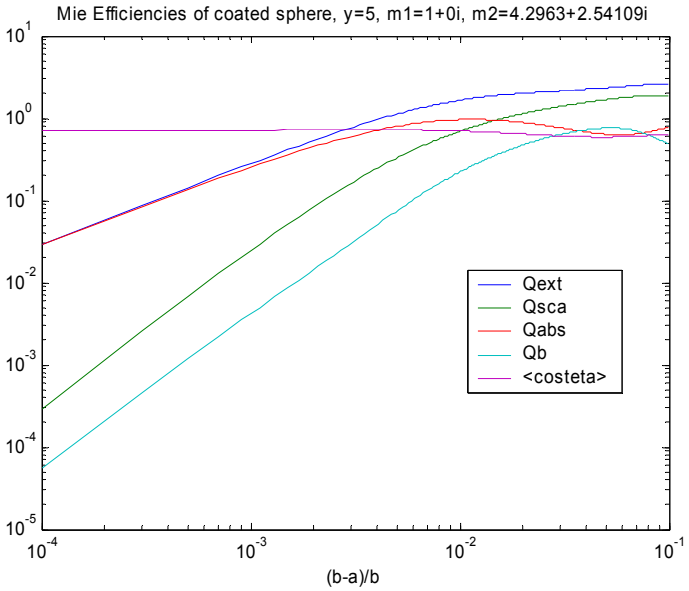

Figure 6: Mie Efficiencies versus relative thickness of coating for water-coated ice sphere of y=5 at 31 GHz, 273K, i.e. b=7.7mm. Note the double-logarithmic scaling.

4.6 Freezing rain

For freezing rain, it is assumed that the ice coating of the rain drops is independent of the drop size. Spectra of propagation constants (Mätzler, 2002b) are computed by the MATLAB Function Miecoated_rain5 (Figure 7)
>> miecoated_rain5(0.1, 4, 273, 1, 100, 30)

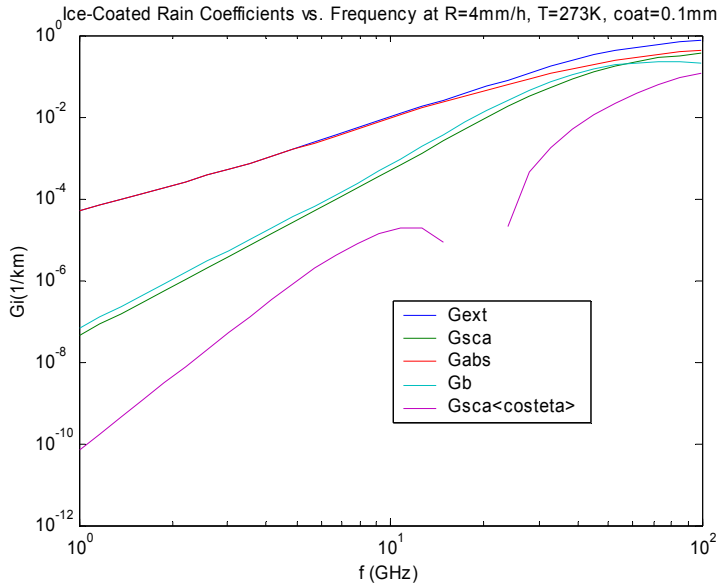

Figure 7: Propagation constants versus frequency for freezing rain with Marshall-Palmer drop-size distribution for R=4mm/h and constant thickness of ice coating of b-a=0.1 mm. Note the double logarithmic scales.

and a plot versus thickness of the ice coating at 31 GHz, R=4mm/h is created by
>> miecoated_rain7(0.1, 4, 273, 1, 100, 30)

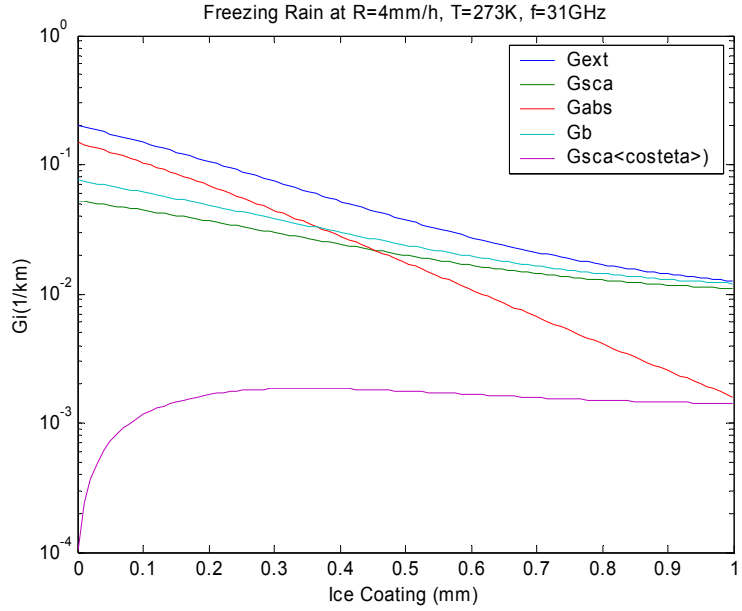

Figure 8: Propagation constants at 31 GHz versus thickness of ice coating for freezing rain with Marshall-Palmer drop-size distribution for R=4mm/h.

4.7 Melting graupel

The opposite to freezing rain is precipitation of melting graupel. Figure 9 shows spectra of a situation with a very thin (0.01mm) liquid layer, assuming a Marshall-Palmer size distribution,
>> miecoated_rain4(0.01,4,273,1,100,10).
Figure 10 shows the dependence on the thickness of the water coating.
>> miecoated_rain6(18,1,273)
A very thin water layer can have a significant contribution to the absorption coefficient, and at 18 GHz, the maximum absorption occurs for a coating of about 0.04mm. Note the lack of symmetry between the opposed situations of Figures 8 and 10.

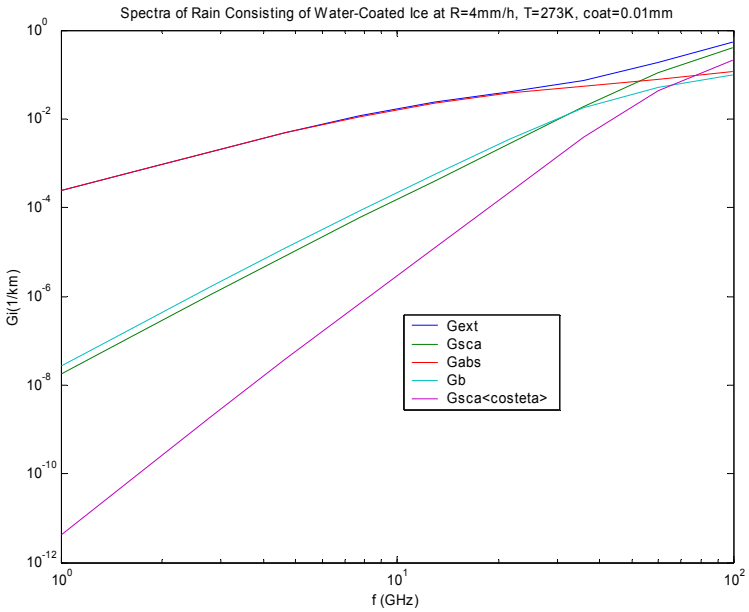

Figure 9: Propagation constants versus frequency for melting graupel at R=4mm/h with Marshall-Palmer size distribution for R=4mm/h and constant thickness of ice coating of b-a=0.01 mm. Note the double logarithmic scales.

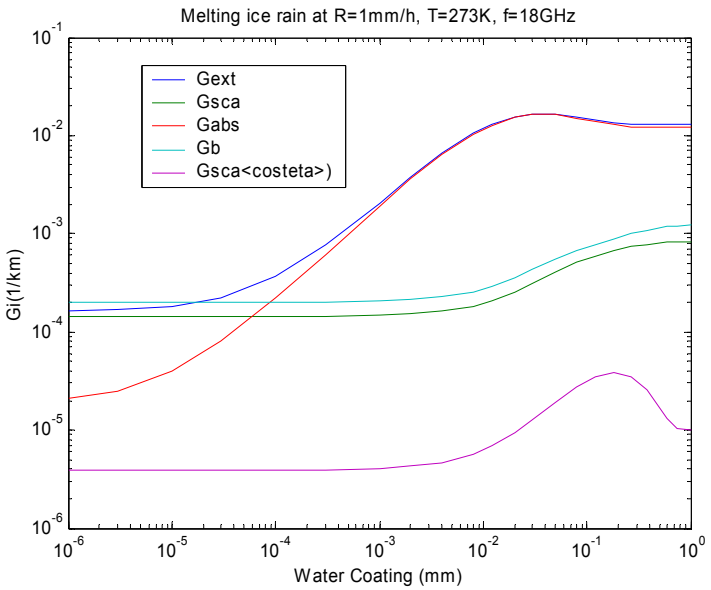

Figure 10: Propagation constants versus thickness of water coating for melting graupel at 18 GHz, R=1mm/h with Marshall-Palmer size distribution.

5 Conclusions

This version of MATLAB Functions for Mie calculations expands on Version 1 (Mätzler, 2002a) by the wider range of parameters allowed in case of non-magnetic spheres, by the addition of functions for magnetic materials and for coated spheres. Furthermore, a deeper analysis of Riccati-Bessel Functions has taken place as a guide for situations in which numerical problems may occur.

The applications of the present work have been concentrated on microwave and millimeter-wave radiation to precipitation in form of rain, freezing rain and melting graupel. As a simplification, it was assumed that the thickness of the coating is not dependent on the particle size. Interesting differences were found between the behaviour of ice spheres coated by liquid water and water spheres coated by ice.

Based on the presented work, the applications can be extended to other particles. As an example, water-coated aerosols can be treated if the complex refractive index

of the core material is known. Furthermore, foam-like materials may be regarded as clouds of hollow spheres.
A related problem, not solved by the present work, is the interaction of radiation with falling snow, both wet and dry. Spherical particles cannot account for the highly non-spherical shape of snow flakes. Nevertheless an approximate solution could be envisaged by using properly selected distribution functions of equivalent coated spheres (Grenfell and Warren, 1999). Other methods are needed if the scatterers are not isotropically oriented (Mätzler, 2002c).

References

Abramowitz M. and I.A. Stegun (eds.), “Handbook of Mathematical Functions”, Dover Publication, New York, NY (1965).

Bohren C.F. and D.R. Huffman, “Absorption and Scattering of Light by Small Particles”, John Wiley, New York, NY (1983).

Chandrasekhar S., "Radiative Transfer", Dover Publication (1960), BEWi TDD 211.

Deirmendjian, D. “Electromagnetic Scattering on Spherical Polydispersions”, American Elsevier, New York, NY (1969).

Grenfell, T., and S.G. Warren, “Representation of a nonspherical ice particle by a collection of independent spheres for scattering and absorption of radiation”, J. Geophys. Res., Vol. 104, pp. 31697-31709 (1999).

Ishimaru A., “Wave propagation and scattering in random media”, Vol. 1, Academic Press, Orlando, FL (1978).

Kong J.A. “Electromagnetic Wave Theory”, John Wiley, New York (1986).

Liebe H.J., G.A. Hufford and T. Manabe, “A model for the complex permittivity of water at frequencies below 1 THz”, Internat. J. Infrared and mm Waves, Vol. 12, pp. 659-675 (1991).

Math Works, “MATLAB User’s Guide”, Natick, MA (1992).

Mätzler C., "Microwave properties of ice and snow", in B. Schmitt et al. (eds.) ”Solar System Ices”, Astrophys. and Space Sci. Library, Vol. 227, Kluwer Academic Publishers, Dordrecht, pp. 241-257 (1998).

Mätzler C. “MATLAB Functions for Mie Scattering and Absorption”, IAP Res. Rep. No. 02-08, June (2002a).

Mätzler C. “Effects of rain on propagation, absorption and scattering of microwave radiation based on the dielectric model of Liebe”, IAP Res. Rep. No. 02-10, June (2002b).

Mätzler C. “Radarsignale von anisotropem Niederschlag ”, IAP Res. Rep. No. 02-2, April (2002c).

Meador W.E. and W.R. Weaver, “Two-Stream Approximations to Radiative Transfer in Planetary Atmospheres: A Unified Description of Existing Methods and a New Improvement”, J. Atm. Sciences, Vol. 37, pp. 630-643 (1980).

Sauvageot H., “Radar Meteorology”, Artech House, Boston, MA (1992).

Appendix: Behaviour of Riccati-Bessel Functions

From the Wronskian, Equation (4.60) of BH

$$\psi_n'\chi_n - \psi_n\chi_n' = 1 \tag{4.60}$$

it follows that the logarithmic derivatives of the Riccati-Bessel Functions ψ_n and χ_n are not independent, but they are related by

$$D_n = \frac{\psi_n'}{\psi_n} = \frac{\chi_n'}{\chi_n} + E_n \tag{A1}$$

where

$$E_n = \frac{1}{\psi_n\chi_n} \tag{A2}$$

is the inverted product. We will also need the ratio F_n, defined by

$$F_n = \frac{\psi_n}{\chi_n} \tag{A3}$$

These Functions of variable $z=mx$ play important roles in Mie Theory. Their behaviour is qualitatively similar at all Orders n; as an example we choose n=10. In the following graphs the functions are presented versus size parameter x for various values of the complex refractive index m. The special characteristics shown enlighten the properties and associated problems of the formulas for the Mie Coefficients.

For better visualisation of the figures to follow, the reader is encouraged to repeat the plotting in MATLAB. Starting with a relatively large, complex m in Figure A1 (m=40+39i) as obtained with the command >> besselplot1(10, 40+39i, 0, 0.01, 350), it is observed that the Riccati-Bessel functions diverge exponentially for linearly increasing x, and the rate of divergence would increase with increasing value of imag(m). (The complex-conjugated quantity $\psi_n^*(z)$ is plotted instead of $\psi_n(z)$, because otherwise the curves would coincide with parts of $\chi_n(z)$).

The function, $\xi_n(z)=\psi_n(z)-i\chi_n(z)$, rapidly converges to 0, indicating that the two Riccati-Bessel Functions are tightly related, i.e. $F_n \to i$ for $x \to \infty$. This follows from the asymptotic expansion of the Hankel Functions (p. 93-94 of BH):

$$\xi_n(mx) = mxh_n^{(1)}(mx) \to (-i)^{n+1}e^{imx} \tag{A4}$$

Thus the absolute values converge to zero as

$$\left|\xi_n(mx)\right| = \to e^{-imag(m)x} \;; \qquad x \to \infty \tag{A5}$$

The data points below the main data band by a factor of about 10^{-15} represent the digital noise generated by the dual-precision computation. The actual values of $\xi_n(mx)$ rapidly decrease and converge to 0 with increasing x as indicated in the x range from 0 to 0.5. Beyond x=0.5 dual precision is not sufficient any more to get accurate values of $\xi_n(mx)$.

There is an symmetry between the convergence of ξ_n and the divergence of its components, $\psi_n(z)$ and $\chi_n(z)$. Because of the insufficient precision this symmetry is not apparent if Figure A1a, but it is very clearly shown in Figure A2a.

The logarithmic derivatives of Figure A1b rapidly converge to –i, but they diverge for $x \to 0$, and they show a special transition, here at $x_{trans} \cong 0.15$, as shown in the Detail Subfigure to A1b. For this transition point we found an approximate behaviour

$$x_{rans} \approx \frac{n}{|real(m)| + |imag(m)|} \tag{A6}$$

In Figure A1c the last term E_n is shown. This function rapidly converges to 0 for increasing x. On the other hand, for $x \to 0$, E_n diverges slightly by z^{-1}

$$E_n(z) = \frac{2n+1}{z}\left(1 + \frac{2z^2}{(2n-1)(2n+3)} + 0(z^4)\right); \ |z| << 1 \tag{A7}$$

whereas ψ_n and χ_n are proportional to z^{n+1} and z^{-n}, respectively, for small z, and thus, the ratio F_n goes as z^{2n+1}.
As examples for smaller values of m, we choose real(m)=2, with imag(m) decreasing from 1 in Figure A2 to 0.09 in Figure A3, to 0 or 0.009, respectively, in Figure A4, and to the negative value, -0.09 in Figure A5. With decreasing imag(m) the exponential divergence of the Riccati-Bessel Functions is weakened, leading to undamped oscillations for real m in Figure A4a. At the same time the logarithmic derivatives become more and more oscillatory, even diverging for certain x values in case of real m. The same is true for the function E_n shown in Figures A2c, A3c, A4c. This means that for real m values, care must be taken when using the functions shown in Figure Parts, b and c. For negative imag(m), in Figure A5a, again an increase of the oscillation amplitude with increasing x is observed, but with a different behaviour of the phase when compared with the same positive imaginary value (Figure A3a).

The following figures were produced by the MATLAB Programs:

besselplot1(n, m, xmin, dx, nx): Computation and plot of Riccati-Bessel Functions of Order n, input: order n, refractive index m, xmin: minimum x value, dx interval, number of x values nx.
besselplot2(n, m, xmin, dx, nx): Computation and plot of logarithmic derivatives of Riccati-Bessel Functions of Order *n* for complex argument *z=m*x*.
besselplot3(n, m, xmin, dx, nx): Computation and plot of Inverse Products E_n of Riccati-Bessel Functions

Furthermore, differences of the logarithmic derivatives of the Riccati-Bessel functions are plotted by

besselplot4(n, m, xmin, dx, nx)

and absolute values of Riccati-Bessel Functions versus x are plotted by

besselplot5(n, m, xmin, dx, nx)

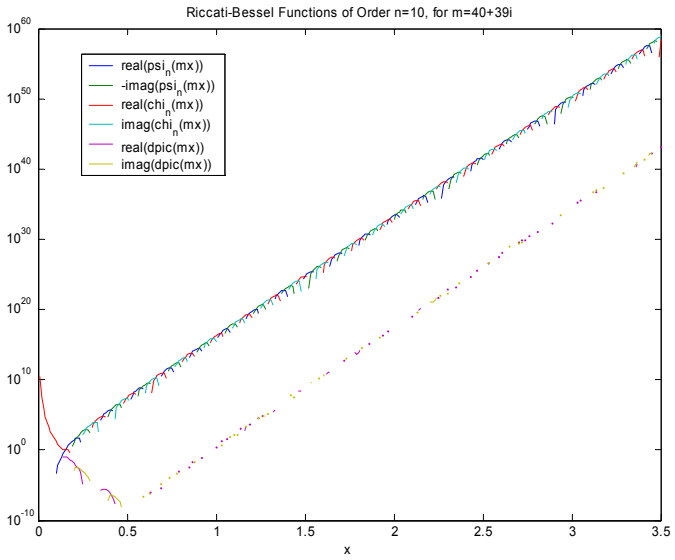

Figure A1a (left):
The complex functions $psi_n=\psi_n^*(z)$, $chi_n=\chi_n(z)$ and $dpic(mx)\equiv\xi_n(mx)=\psi_n(z)-i\chi_n(z)$ versus x, for $z=mx$, n=10 and m=40+39i, using a logarithmic y axis, ignoring negative function values.

Figure A1b (left below):
The ratios $D_n=\psi_n'(z)/\psi_n(z)$, $D_{nch}=\chi_n'(z)/\chi_n(z)$ versus x, for $z=mx$, n=10 and m=40+39i, using a linear y axis. These functions converge towards 0–i for increasing x, and they diverge for $x\rightarrow 0$.

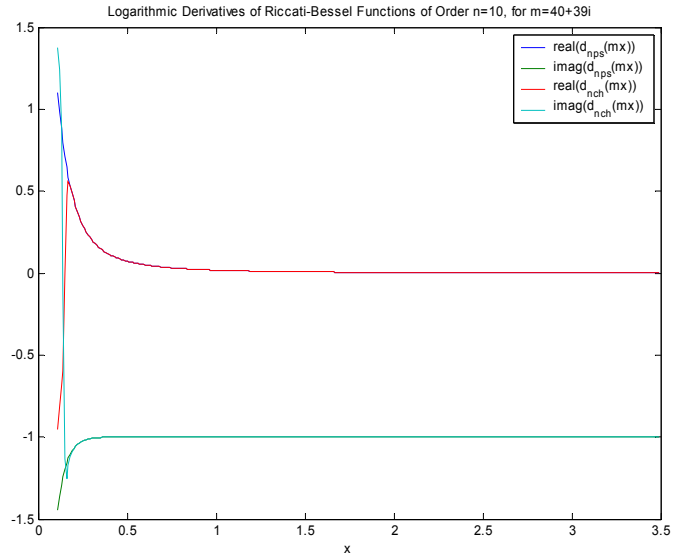

Detail to Fig. A1b for x= 0.05 to 0.25

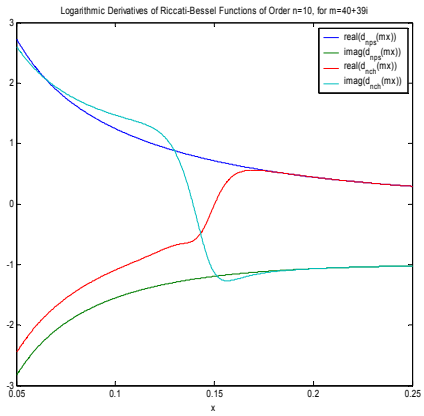

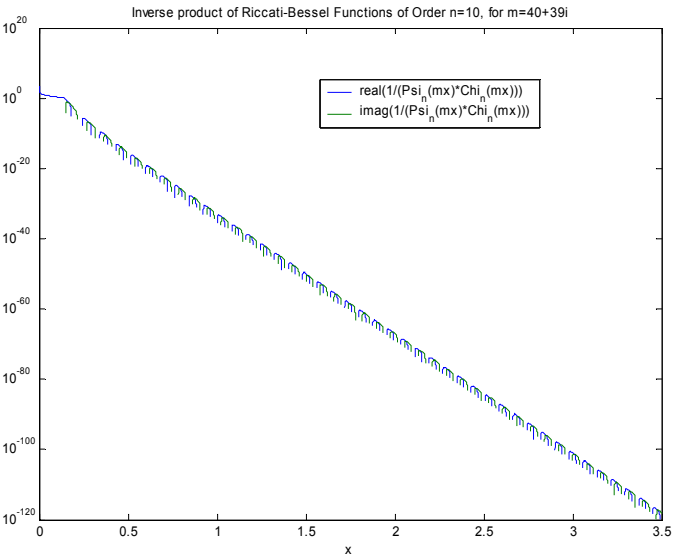

Figure A1c (left):
The inverted product $E_n(z)=1/[\psi_n(z)\chi_n(z)]$, versus x, for $z=mx$, n=10 and m=40+39i, using a logarithmic y axis, ignoring negative function values.

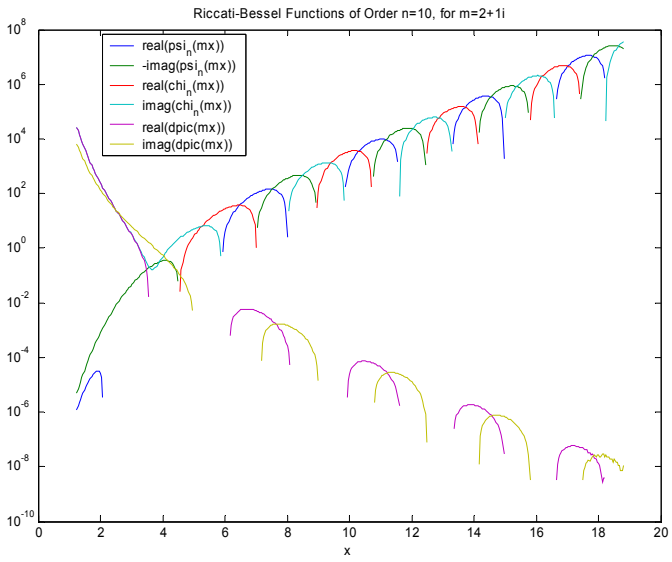

Figure A2a (left):
The complex functions $psi_n=\psi_n^*(z)$, $chi_n=\chi_n(z)$ and $dpic(mx)\equiv\xi_n(mx)=\psi_n(z)-i\chi_n(z)$ versus x, for $z=mx$, $n=10$ and $m=2+i$, using a logarithmic y axis, ignoring negative function values. Whereas $\psi_n(z)$ only diverges for large x, $\chi_n(z)$ also diverges for $x\rightarrow 0$.

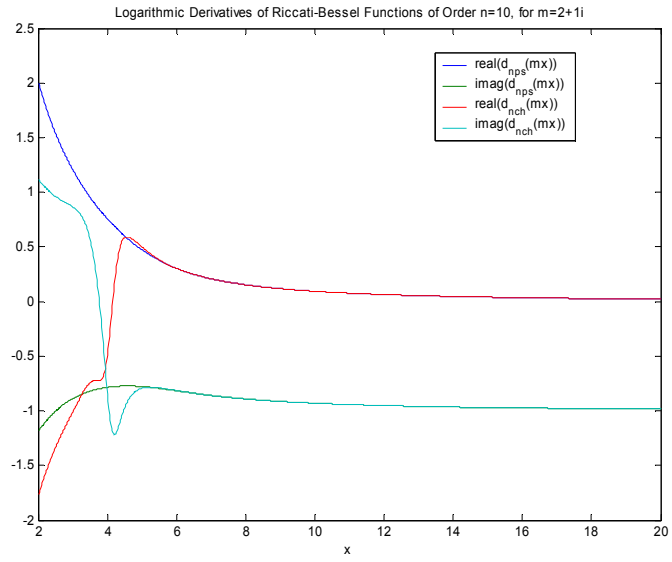

Figure A2b:
The ratios $D_n=\psi_n'(z)/\psi_n(z)$, $D_{nch}=\chi_n'(z)/\chi_n(z)$ versus x, for $z=mx$, $n=10$ and $m=2+i$, using a linear y axis. These functions converge towards 0–i for increasing x, and they diverge for $x\rightarrow 0$.

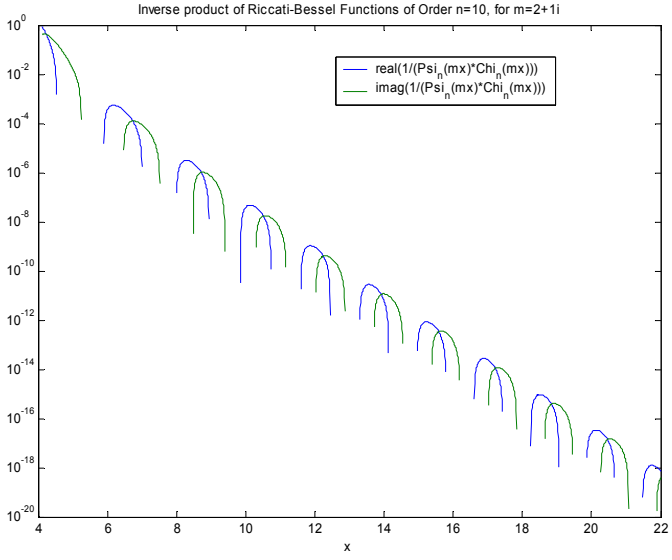

Figure A2c:
The inverted product $E_n(z)=1/[\psi_n(z)\chi_n(z)]$, versus x, for $z=mx$, $n=10$ and $m=2+i$, using a logarithmic y axis, ignoring negative function values.

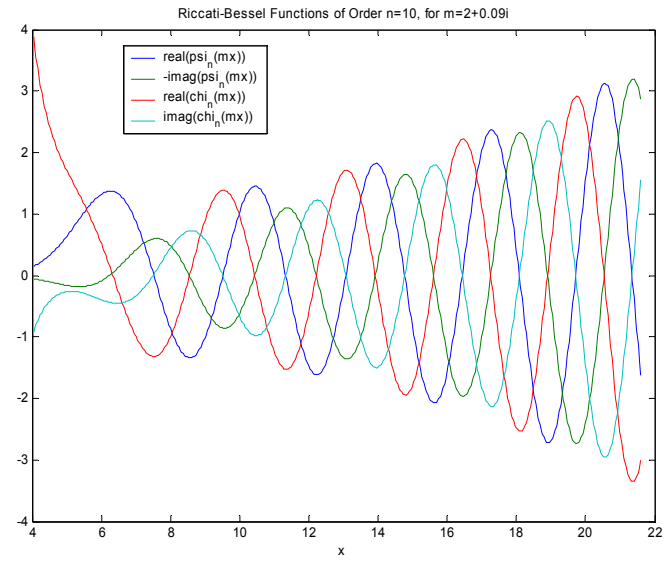

Figure A3a (left):
The complex functions $psi_n=\psi_n^*(z)$ and $chi_n=\chi_n(z)$ versus x, for $z=mx$, $n=10$ and $m=2+0.09i$.

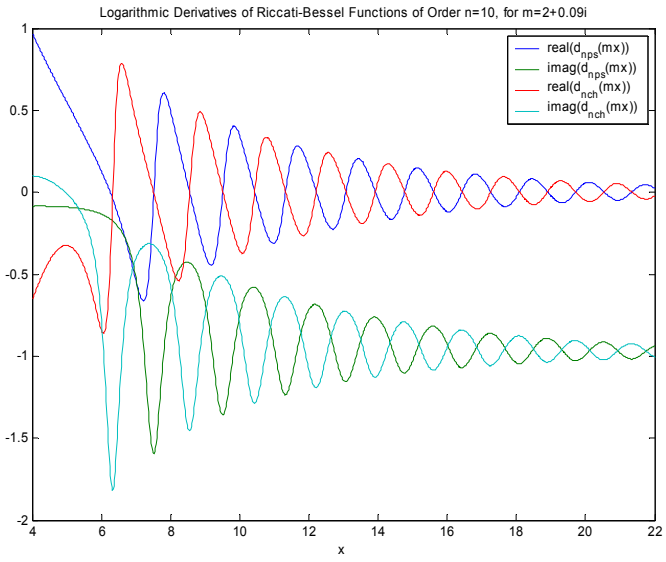

Figure A3b:
The ratios $D_n=\psi_n'(z)/\psi_n(z)$, $D_{nch}=\chi_n'(z)/\chi_n(z)$ versus x, for $z=mx$, $n=10$ and $m=2+0.09i$.

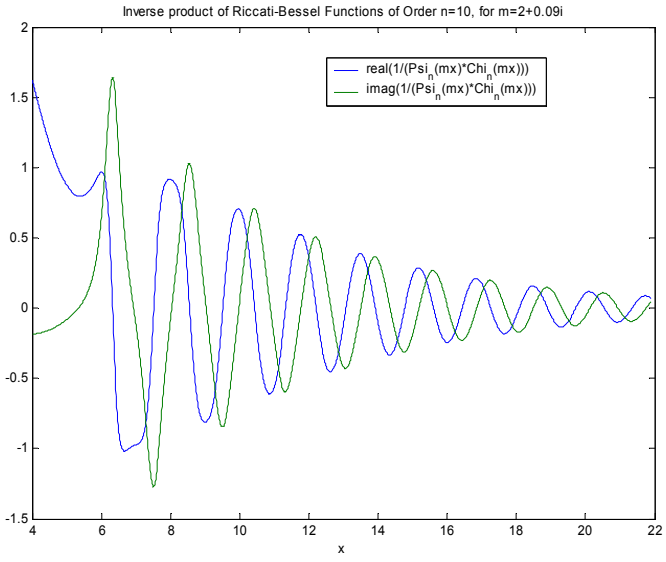

Figure A3c:
The inverted product $E_n(z)=1/[\psi_n(z)\chi_n(z)]$, versus x, for $z=mx$, $n=10$, and $m=2+0.09i$.

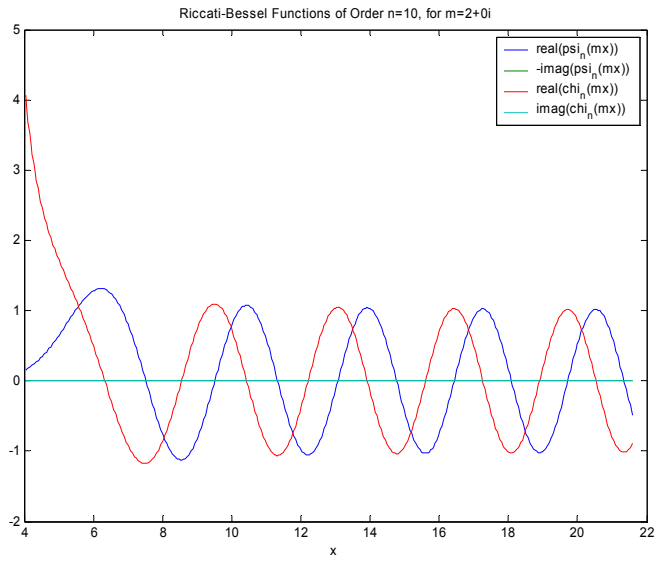

Figure A4a (left):
The functions $psi_n=\psi_n^*(z)$, $chi_n=\chi_n(z)$ versus x, for $z=mx$, $n=10$ and $m=2$; These are real, undamped oscillations, similar to sine and cosine functions (imaginary parts are zero for real m).

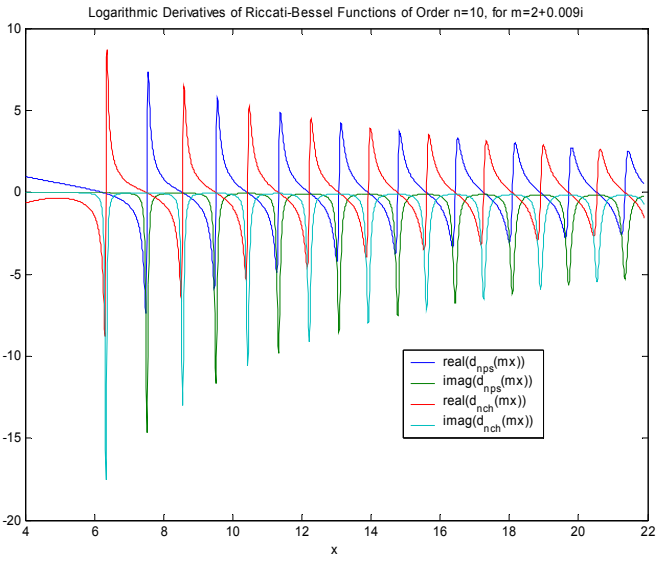

Figure A4b (left, below):
The ratios $D_n=\psi_n'(z)/\psi_n(z)$, $D_{nch}=\chi_n'(z)/\chi_n(z)$ versus x, for $z=mx$, $n=10$ and $m=2+0.009i$.

Detail to Figure A4b, here for $x=6$ to 10, but with $m=2+0.001i$:

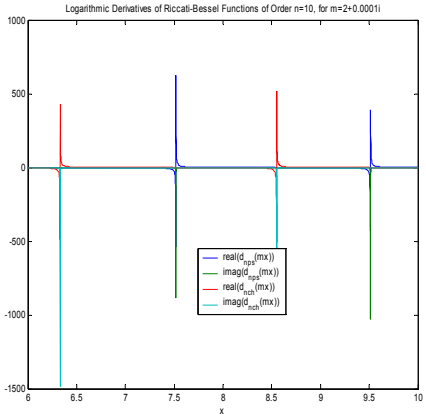

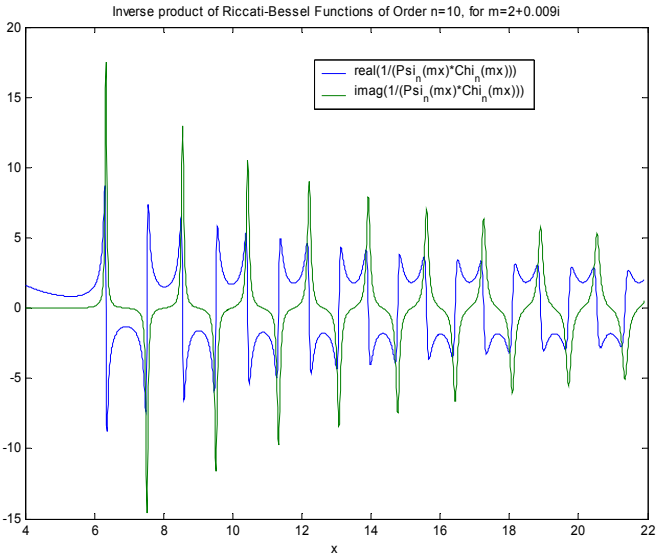

Figure A4c (left):
The inverted product $E_n(z)=1/[\psi_n(z)\chi_n(z)]$, versus x, for $z=mx$, $n=10$ and $m=2+0.009i$.

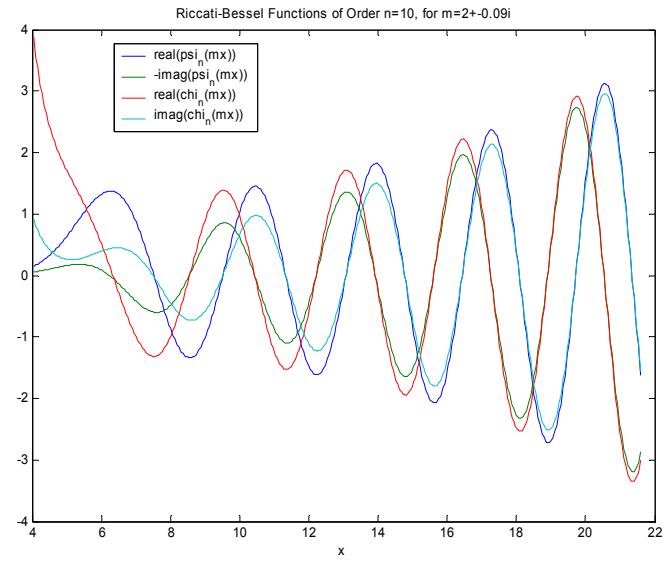

Figure A5a (left):
The complex functions $psi_n=\psi_n^*(z)$, $chi_n=\chi_n(z)$ versus x, for $z=mx$, n=10 and m=2-0.09i (meaning amplification).

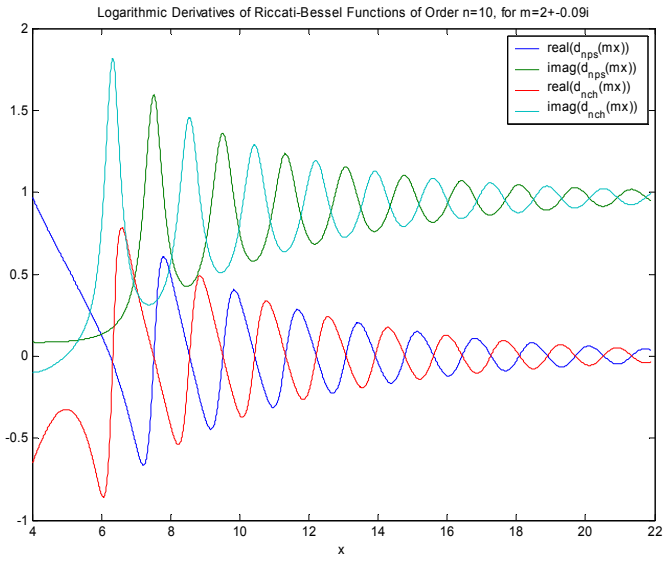

Figure A5b (left):
The ratios $D_n=\psi_n'(z)/\psi_n(z)$, $D_{nch}=\chi_n'(z)/\chi_n(z)$ versus x, for $z=mx$, n=10 and m=2-0.09i.

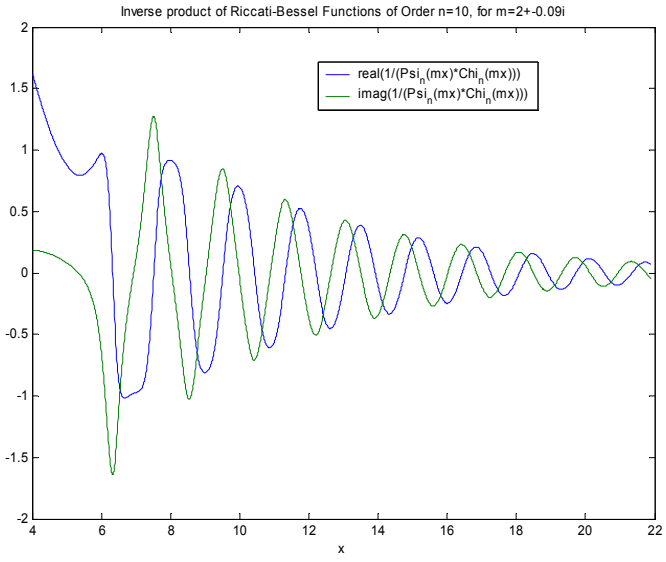

Figure A5c (left):
The inverted product $E_n(z)=1/[\psi_n(z)\chi_n(z)]$, versus x, for $z=mx$, n=10 and m=2-0.09i.